RESEARCH ARTICLE

Key Points:
- The changes in surface forcing induce a weakening of the large-scale circulation which systematically modulates the transition process
- The transition from suppressed to active convection is delayed considerably when convection interacts with the large-scale circulation
- The interactions between convection and large-scale circulation are strongly affected by the value of convective entrainment rate

Correspondence to:
C. L. Daleu,
c.daleu@reading.ac.uk,
chimenedaleu@yahoo.fr

Using the Weak-Temperature Gradient Approximation to Evaluate Parameterizations: An Example of the Transition From Suppressed to Active Convection

C. L. Daleu[1] , R. S. Plant[1] , and S. J. Woolnough[1]

[1]National Centre for Atmospheric Science, Department of Meteorology, University of Reading, Reading, UK

Abstract Two single-column models are fully coupled via the weak-temperature gradient approach. The coupled-SCM is used to simulate the transition from suppressed to active convection under the influence of an interactive large-scale circulation. The sensitivity of this transition to the value of mixing entrainment within the convective parameterization is explored. The results from these simulations are compared with those from equivalent simulations using coupled cloud-resolving models. Coupled-column simulations over nonuniform surface forcing are used to initialize the simulations of the transition, in which the column with suppressed convection is forced to undergo a transition to active convection by changing the local and/or remote surface forcings. The direct contributions from the changes in surface forcing are to induce a weakening of the large-scale circulation which systematically modulates the transition. In the SCM, the contributions from the large-scale circulation are dominated by the heating effects, while in the CRM the heating and moistening effects are about equally divided. A transition time is defined as the time when the rain rate in the dry column is halfway to the value at equilibrium after the transition. For the control value of entrainment, the order of the transition times is identical to that obtained in the CRM, but the transition times are markedly faster. The locally forced transition is strongly delayed by a higher entrainment. A consequence is that for a 50% higher entrainment the transition times are reordered. The remotely forced transition remains fast while the locally forced transition becomes slow, compared to the CRM.

1. Introduction

In the tropics, deep convection and cloud-related processes are closely linked with the large-scale circulation. Thus, a good representation of the interactions between tropical deep convection and large-scale circulations in numerical models is essential to understand and to simulate tropical climate and its variability. General circulation models (GCMs) still rely heavily on parameterizations. These parameterizations are often developed in single-column model (SCM) framework and then implemented in GCMs. The weak-temperature gradient (WTG) approach offers an opportunity to test these parameterizations in a simple framework which allows the two-way interactions between convection and large-scale circulation to develop, without the complexities of the full GCM.

CRM and SCM simulations with a predefined large-scale flow are computationally cheap ways to simulate the effects of a large-scale circulation on convection. Such simulations have provided much useful insight. For instance, Petch et al. (2007) proved that the SCM simulations with predefined large-scale horizontal winds were able to reproduce some examples of biases seen in the full numerical weather prediction (NWP) model. However, such simulations cannot be used to understand the factors that control the occurrence and intensity of tropical deep convection (Sobel et al., 2004), because the rain rates produced are constrained due to the predefined large-scale moisture advection (Mapes, 1997; Sobel & Bretherton, 2000). It is not appropriate to ignore the feedback of convection on the large-scale flow, particularly in nonequilibrium conditions (e.g., Holloway & Neelin, 2009; Mapes, 1997; Masunaga, 2012).

The WTG approach of Sobel and Bretherton (2000) has proved to be a useful framework to represent the feedback of convection to the large-scale flow in a limited-area model, representing a region of the atmosphere near the equator. The physical principle considered is that gravity waves over a large area of the

tropics rapidly redistribute density anomalies toward near-uniform density on isobaric surfaces (Bretherton & Smolarkiewcz, 1989; Mapes & Houze, 1995; Yano & Bonazzola, 2009).

Studies which apply the WTG approach parameterize a large-scale circulation which interacts with the simulated convection, using the constraint that temperature anomalies of all vertical wavenumbers are equally damped through a specified time scale (e.g., Daleu et al., 2012; Raymond & Zeng, 2005; Sessions et al., 2010; Sobel & Bretherton, 2000; Sobel et al., 2007; and others, including the present study). An alternative approach is the spectral WTG, for which temperature anomalies are decomposed in the vertical dimension and damped proportionally to the phase speed of individual vertical wavenumbers. It is an innovation of the WTG which was recently proposed by Herman and Raymond (2014). There is another large-scale parameterization approach, namely, the damped gravity wave (DGW), which is based on the coupling of convection to a linear gravity wave of a single horizontal wavenumber (e.g., Daleu et al., 2015b, 2016; Edman & Romps, 2013; Kuang, 2014, 2011; Romps, 2005, 2012b).

Previous studies using these large-scale parameterization approaches have found some differences in the shape of the derived large-scale vertical velocities. The DGW approach often produces large-scale vertical velocities that are less top-heavy and are smoother than those produced using the WTG approach (e.g., Daleu et al., 2016; Wang et al., 2013). Moreover, Wang et al. (2016) demonstrated that in comparison to the WTG and DGW approaches, the spectral WTG approach better captures the vertical structure of the large-scale vertical motion observed during the DYNAMO field campaign. Although the spectral WTG approach has become more popular, we used the WTG approach because it matches the approach used in the CRM study of Daleu et al. (2015b), to which this study is compared.

The WTG approach is normally applied using a configuration that couples an interactive column to a reference reservoir column (reference column approach). Recently, Daleu et al. (2012) extended the reference column approach to a coupled-column approach which considers two interactive columns, fully coupled via a parameterized large-scale circulation. The coupled-column approach was proposed as a methodology for studying the influence on local convection of changes in remote convection. It has been used by Daleu et al. (2015b) to investigate the role of an interactive large-scale circulation in modulating the transition from suppressed to active convection, that is forced locally or remotely. Daleu et al. (2015b) found that the transition to deep convection is delayed in the presence of the WTG-derived large-scale circulation. The transition to deep convection occurred more slowly over a time scale that characterized changes in the strength of the large-scale circulation that might develop over a warm pool. They also found the transition process to be slower in experiments that are forced by changes in the remote surface conditions, compared to experiments that are forced by changes in the local surface conditions.

Various studies have investigated transitions from suppressed to active convection forced by changes in the local surface conditions (e.g., Khairoutdinov & Randall, 2006; Kuang & Bretherton, 2006; Sobel & Bretherton, 2000; Wu et al., 2009). The use of a coupled-column configuration allows the consideration of an evolving large-scale circulation during the transition process, and allows transitions from suppressed to active convection to be forced by changes in the remote surface conditions. The starting point of the experiments performed here and in Daleu et al. (2015b) is a situation in which a large-scale circulation driven by inhomogeneous SST in two distinct regions of the tropical atmosphere suppresses convection in its descending branch and enhances convection in its ascending branch. The large-scale circulation is then removed by equalizing the SST between the two regions. This is done by either increasing SST in the suppressed-convection region, reducing SST in the enhanced-convection region, or a combination of both. For each of the forcing methods, we will examine the transient evolution of convection from a suppressed to a more active phase under the influence of a diminishing, and ultimately a vanishing large-scale circulation.

While Daleu et al. (2015b) used a CRM to determine convective properties in each column of the coupled-column approach, this study uses a SCM. Therefore, a new feature of this study is a direct comparison of the transition experiments performed using the SCM (this study) against the equivalent transition experiments performed using the CRM (the study of Daleu et al., 2015b).

Daleu et al. (2015a, 2016) performed a direct comparison of the behavior of a set of SCMs against that of a set of CRMs when using the WTG approach and the DGW approach to couple a simulated column to a reference state. They demonstrated that with exactly the same implementation of the WTG or DGW approach, the behavior of CRMs are more consistent while there is much larger intermodel variability among SCMs.

Raymond (2007) is the first study that used the WTG approach to evaluate convective parameterizations. Here we will demonstrate that the comparisons between SCMs and CRMs when using the WTG approach may be used to assess the ability of the SCM parameterized physics to capture the interactions between convection and large-scale circulations, and so that the results from such assessments may be useful for evaluating convective parameterizations.

The simulations of large-scale circulation and associated variability in state-of-art GCMs display a wide range of results (Lin et al., 2008), particularly because of different convective parameterization schemes used. The entrainment rate is a parameter in the convection scheme that is well known to be an important source of model uncertainty, and to influence the simulation of the tropical mean climate (e.g., Bush et al., 2015; Oueslati & Bellon, 2013) and variability (e.g., Klingaman & Woolnough, 2014). In this study, we will explore the sensitivity of the simulated transition to increased convective entrainment rate within the SCM.

This paper is organized as follows. Section 2 describes the SCM used and presents its radiative-convective equilibrium state (RCE) states for various SSTs. Section 3 gives brief details of the implementation of the WTG approach in order to couple two interactive columns. The same section presents the equilibrium states of the coupled-column simulations over nonuniform SST, which are later used as initial conditions for the simulations of the transition. It also presents the equilibrium states of the coupled-column simulations over uniform SST, which are expected to be the final states after the transition. Section 4 presents the main results of simulations using the local, remote, and local-and-remote forced transition methods. In the same section, the relative contributions of surface forcing and the large-scale circulation are determined. The impacts of changes in entrainment rates are highlighted in section 5 and a summary of the main findings is presented in section 6.

2. Model Description and Radiative-Convective Simulations

2.1. Model Description

All numerical experiments in this study are conducted using a SCM form of the Met Office's general circulation model (Davies et al., 2005) at version 7.8 (UMv7.8). More precisely, we use choices and parameter settings corresponding to the Global Atmosphere version 3.0 (GA3.0) configuration of the atmospheric component of the HadGEM family of models (Walters et al., 2011). The convection parameterization is based on the bulk mass-flux approach of Gregory and Rowntree (1990), with various subsequent modifications described by Derbyshire et al. (2011), including a smooth adaptive detrainment specification. Stratiform clouds are represented using the prognostic PC2 scheme of Wilson et al. (2008) with the associated microphysics following Wilson and Ballard (1999). The boundary layer parameterization is that of Lock et al. (2000).

A particular interest of this study is to assess the impact of increased convective entrainment rate in the modified Gregory and Rowntree (1990) convection scheme used in above UM configuration. The fractional mixing entrainment rate profile for midlevel convection (convection starting above the boundary layer) and for deep convection is parameterized as:

$$\varepsilon(z) = 4.5F \frac{gp(z)\rho(z)}{p_*^2}, \tag{1}$$

ε is expressed per unit length and its full description is given in Gregory and Rowntree (1990). g is the acceleration due to gravity. p and ρ are the pressure and density as a function of height, and p_* is the pressure at the surface. F is an entrainment factor that controls midlevel and deep entrainment. Unless otherwise stated, we use the standard GA3.0 value of entrainment factor, F=0.9. ε is increased by increasing F and experiments to assess sensitivities to higher entrainment factors are presented in section 5.

Increasing ε also increases the mixing detrainment rate for deep convection, δ_m:

$$\delta_m(z) = 1.5[1 - RH(z)]\varepsilon(z), \tag{2}$$

δ_m is related to ε by the relative humidity, RH, and δ_m exceeds ε when RH < 1/3. At the level of neutral buoyancy, the parcel is forced to detrain completely without overshooting. Further details of the detrainment formulation are given in Stratton et al. (2009) and Derbyshire et al. (2011).

The model is configured with 63 levels in the vertical, on a stretched grid with finer resolution closer to the surface. The lower boundary is an ocean surface with a prescribed time-dependent SST, and the Coriolis force is zero. The top and bottom of the domain are rigid lids and a Newtonian damping layer is used above 15 km. The parameters used to setup this SCM have the values set in the GA3.0 default configuration (Walters et al., 2011).

Aside from any large-scale circulation which might develop, the SCM is forced with an idealized cooling that represents the combined effects of shortwave and longwave radiation. Such cooling is prescribed but will henceforth be referred to as the radiative cooling. The cooling rate is 1.5 K d^{-1} up to 12 km and it then decreases linearly in height to reach the prescribed value of 0 K d^{-1} at 15 km. The horizontal wind speed components are relaxed toward vertically uniform values of 0 and 5 m s^{-1}, both with the relaxation time scale of 6 h, consistent with the setup in Daleu et al. (2015b).

2.2. Radiative-Convective Equilibrium Simulations

In this section, we show the results from radiative-convective equilibrium (RCE) simulations performed with SSTs of 300.7, 301.7, 302.7, 303.7, and 304.7 K. Each simulation is initialized with temperature and humidity profiles measured during the Tropical Ocean and Global Atmosphere Coupled Ocean Atmosphere Response Experiment (TOGA COARE) from the western Pacific warm pool (Webster & Lukas, 1992). The simulations are run for 100 days, and averages over the last 40 days are used to define the model state and statistics at equilibrium.

Each simulation achieves an equilibrium state in which precipitation balances surface evaporation; that is the RCE state. Figure 1 shows the potential temperature and specific humidity profiles of the RCE state at 302.7 K. It also shows the deviation from the RCE profiles at 302.7 K for the set of RCE simulations with SSTs of 300.7, 301.7, 303.7, and 304.7 K. The column is warmer and moister for warmer SST and the resulting potential temperature and specific humidity profiles are smoother than those produced using the CRM [compare Figure 1 with Figure 2 of Daleu et al. (2012)). These simulations are used to provide a set of initial profiles for the simulations described in section 3.
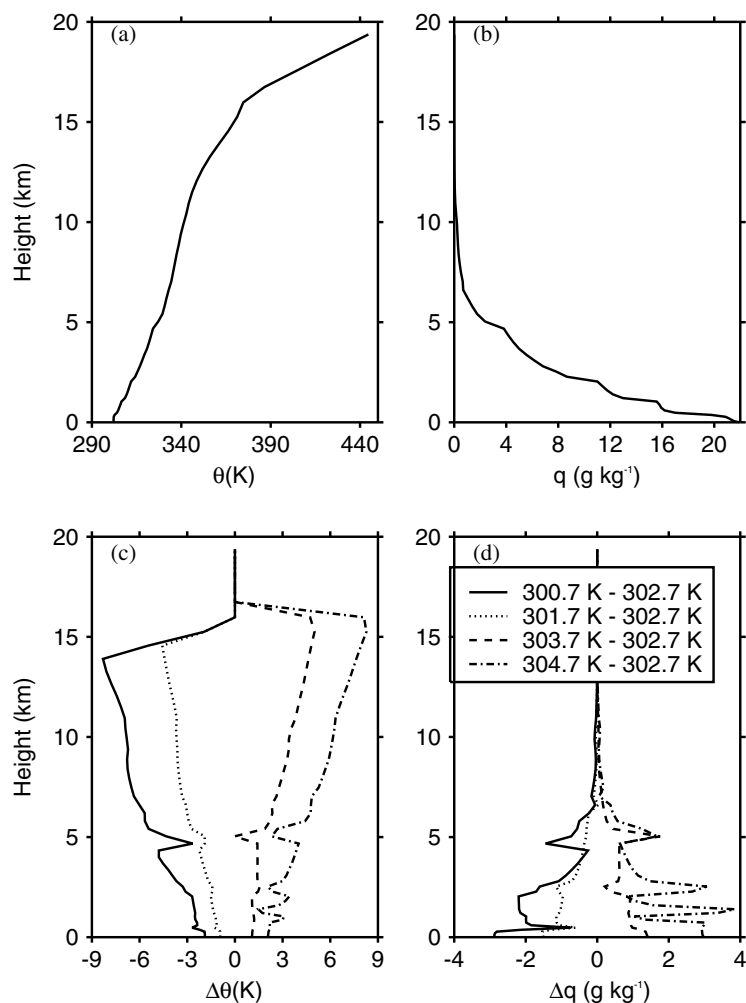
3. Coupled-Column Simulations

3.1. Coupled-Column Configuration

The coupled-column configuration follows that of Daleu et al. (2015b) and represents two simulated columns that are fully coupled via the WTG approach. The subscripts 1 and 2 are used to label the horizontal-domain-mean properties in columns 1 and 2, respectively. In the free troposphere, the large-scale vertical velocities, $\bar{w}_1$ and $\bar{w}_2$ act to reduce the difference in horizontal-domain-mean potential temperature between columns 1 and 2, over a specified WTG coupling time scale τ. That is:

$$\bar{w}_2 \frac{\partial \bar{\theta}_2}{\partial z} - \bar{w}_1 \frac{\partial \bar{\theta}_1}{\partial z} = \frac{\bar{\theta}_2 - \bar{\theta}_1}{\tau}. \tag{3}$$

Separate expressions for $\bar{w}_1$ and $\bar{w}_2$ are obtained by applying the two-column form of the mass continuity equation. That is:

$$\bar{w}_1 + \bar{w}_2 = 0. \tag{4}$$

The simulations discussed in this paper are performed with $\tau = 2$ h, which is the value used in the same idealized experimental setup using a CRM (Daleu et al., 2015b).

Figure 1. (a) Potential temperature and (b) specific humidity profiles for the RCE state of the SCM with an SST of 302.7 K. Also shown are the deviations from the RCE profiles at 302.7 K of (c) potential temperature and (d) specific humidity for the RCE simulations with SSTs of 300.7, 301.7, 303.7, and 304.7 K.
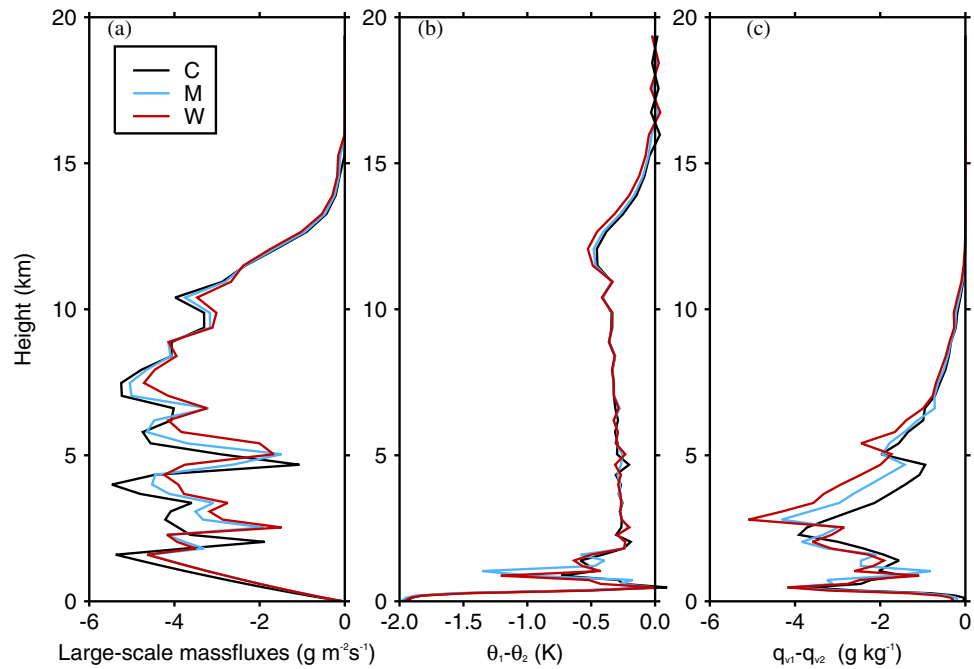
Figure 2. (a) Large-scale mass flux for column 1, and (b) potential temperature and (c) specific humidity differences between columns 1 and 2. The profiles are for the simulations listed in Table 1. The large-scale mass flux is computed as the product of density and the WTG-derived large-scale vertical velocity.

$\bar{w}_1$ and $\bar{w}_2$ are set to zero at model levels above 15.25 km. We follow Sobel and Bretherton (2000) and choose a nominal boundary layer top of 1.5 km, below which we calculate the WTG vertical velocity by interpolating linearly in height between the value diagnosed at the first model level above 1.5 km to the prescribed value of zero at the surface.

The WTG approach is only one way to parameterize the large-scale circulation and other parameterizations of the large-scale dynamics, including the spectral WTG approach or the DGW approach are available. While the results of particular sensitivity tests may be different the principle of using such an approach to compare CRM and SCM remains valid. Here we used the WTG approach because it matches the approach used in the CRM study of Daleu et al. (2015b). The large-scale velocities $\bar{w}_1$ and $\bar{w}_2$ introduce additional source and sink terms to the heat and moisture tendencies. By using an upwind advection scheme for the horizontal advection, the large-scale advective tendency for the horizontal-domain-mean quantity $\bar{\chi}_1$ is given by

$$\left(\frac{\partial \bar{\chi}_1}{\partial t}\right)_{WTG} = \frac{\chi_*}{\bar{\rho}}\frac{\partial}{\partial z}(\bar{\rho}\bar{w}_1) - \frac{1}{\bar{\rho}}\frac{\partial}{\partial z}(\bar{\rho}\bar{w}_1\bar{\chi}_1). \tag{5}$$

and similarly for $\bar{\chi}_2$. Here χ_* is the appropriate upwind value for $\bar{\chi}$. The first term on the right-hand side is obtained based on the horizontal convergence, under the assumption that the horizontal flow at each model level is either all into or all out of each column. Equation (5) is applied to potential temperature and water vapor only and is not applied to any form of hydrometeor. A full derivation of equation (5) is given in Daleu et al. (2012).

Table 1
Values of SST (K) for Columns 1 and 2

Experiments	C	M	W
SST$_1$	300.7	301.7	302.7
SST$_2$	302.7	303.7	304.7
MRR$_1$	0.12	0.25	0.19
MRR$_2$	10.70	10.72	10.90

Note. Also given are the values of mean rain rates (MRR in mm d^{-1}) obtained at equilibrium in the simulations.

3.2. Coupled-Column Simulations Over Nonuniform SST

In this section, we show the results from three simulations performed using the coupled-column approach with the SST difference of 2 K between the columns (see Table 1). In each case, column 1 is chosen to be colder than column 2. These simulations have different values of mean SST and are classified as C, M, and W for cold, medium, and warm respectively. Each simulation is run for 100 days, and averages over the last 40 days are used to define the model state and statistics at equilibrium.

Each column of the simulations C, M, and W is initialized with the profile obtained in the previous RCE simulations for the given SST. Figure 2a shows the large-scale mass flux profiles obtained at equilibrium for column 1. The large-scale mass flux is calculated as the product of density and the WTG-derived large-scale vertical velocity. For each simulation, the absolute difference in SST drives an overturning circulation with its descending branch being in column 1. For these three simulations, the strength and the vertical structure of the large-scale circulation at equilibrium are very similar. These large-scale mass fluxes are not so top-heavy as those obtained in equivalent simulations using the CRM. For instance, between 5 and 11 km, the large-scale mass flux in the SCM is roughly constant (see Figure 2a), while in the CRM it increases by a factor of 2.5 (see Figure 4 of Daleu et al., 2015b). From previous studies, models that apply the WTG approach often produce large-scale vertical mass fluxes that are top-heavy when compared with those produced using the DGW approach (Daleu et al., 2016; Wang et al., 2013).

These large-scale mass fluxes are noisy in the vertical. A similar result was obtained with other SCMs when using the WTG approach to couple a simulated column to a reference state (Daleu et al., 2016), while simulations which apply the spectral WTG and DGW produce smoother profiles (e.g., Daleu et al., 2016; Herman & Raymond, 2014; Wang et al., 2016). Using the WTG approach, temperature anomalies of all vertical wave numbers are equally damped through the same WTG coupling time scale, and any high vertical wave number structures in the temperature will be reflected in the vertical velocity profile. The spectral WTG approach overcomes this issue since the high wavenumbers are damped with a much longer time scales.

Figures 2b and 2c show the difference in potential temperature and specific humidity profiles between columns 1 and 2. In the boundary layer, the horizontal temperature differences are relatively large compared to those in the free troposphere, where the WTG-derived large-scale circulation constrains the temperature profiles of the two columns to remain close to each other. As a result, the horizontal temperature difference in the free troposphere has a maximum value of 0.5 K (Figure 2b), compared to the value of about 8 K obtained in the RCE simulations of this SCM with 2 K difference in SST (e.g., solid curve in Figure 1c). The warming and drying effects from the large-scale descent inhibit convection in column 1 while the compensating cooling and moistening effects from the large-scale ascent enhance convection in column 2. As a result, column 1 is dominated by shallow nonprecipitating convection and the relatively low precipitation rate in column 1 (with respect to the value in column 2) is produced by large-scale rain from stratiform clouds at the top of the boundary layer.

In the ascending column, the humidity profiles remain near the profile of the corresponding RCE state. In contrast, humidity profiles of the descending column are much drier compared to that of the corresponding RCE state. For instance, the differences in column relative humidity with respect to the value of the RCE state are −11% in the descending branch compared to 3% in the ascending branch. Hence, the difference in humidity profiles between columns 1 and 2 (Figure 2c) is mainly the result of drying in the descending column.

Despite the fact that the simulations C, M, and W have different values of mean SST in the system, the mean statistics achieved at equilibrium are very similar for the whole domain. Similar to the results of Ramsay and Sobel (2011) and Wang and Sobel (2011), the local rain rate is not determined by the value of mean SST in the system. Rather, it is determined by the difference of SSTs between the columns. For example, the mean rain rates in each column are very similar between experiments (values in the fourth and fifth rows of Table 1) consistent with the large-scale vertical velocity (Figure 2a) and the large-scale cooling, and consistent with the potential temperature difference between the columns (Figure 2b). The mean rain rate in column 1 is relatively small while the mean rain rate in column 2 is almost twice the mean value of 5.53 mm d^{-1} obtained in the RCE simulations with various values of SSTs.

3.3. Multiple Precipitating Equilibria in the Coupled SCMs

In this section, we show the results from the coupled-column model over a uniform SST. The model states from these experiments are expected to correspond to the final states of the transition experiments analyzed in sections 4 and 5. To compare the equilibrium states achieved in the coupled-column simulations over uniform SST with the RCE simulation with an SST of 302.7 K, we analyzed the heating rates from the large-scale circulation at equilibrium in column 1. That is H_{ls_1}. Here we consider an equilibrium state to have approximately zero mean large-scale circulation if $|H_{ls_1}| < 0.1$ mm d^{-1}.

The SSTs in columns 1 and 2 are 302.7 K and we performed simulations in which both columns are initialized with the mean profiles from the RCE state with an SST of 302.7 K (Figures 1a and 1b). The columns
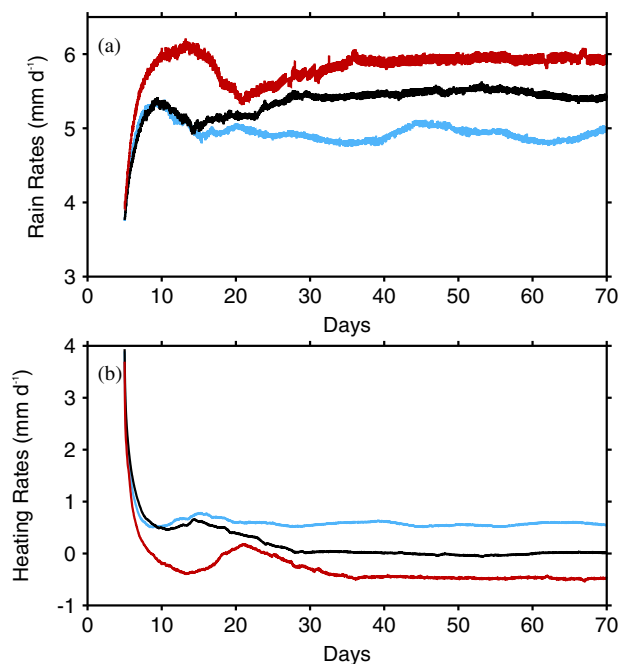
Figure 3. Time series of the 5 day running mean and ensemble mean (a) rain rates and (b) column-integrated heating rates from the large-scale circulation. The results are for column 1 of coupled-column simulations with uniform SST which result in approximately zero large-scale circulation in the system (black curve), weak large-scale ascent in column 1 (red curve), and weak large-scale descent in column 1 (blue curve). The initial conditions are taken from different instantaneous states at equilibrium of the RCE simulations with SSTs of 300.7 and 302.7 K.

produce an equilibrium state with approximately zero mean large-scale circulation since $H_{ls_1} = 0.07$ mm d^{-1} (results not shown).

To examine the sensitivity to the initial conditions, we performed a set of ten simulations in which column 1 is initialized with different instantaneous profiles at equilibrium of the RCE simulation with an SST of 300.7 K. The coupled-column model run over uniform SST produces multiple precipitating equilibria, and these are grouped in three subsets according to the type of equilibrium state achieved in column 1. Figure 3 shows the time evolution of mean rain rates and column-integrated heating rates from the large-scale circulation. The results are the ensemble-means from simulations producing each type of equilibrium state. As well as an equilibrium state with approximately zero mean large-scale circulation in the system, which is obtained in four simulations, the other six simulations produced equilibrium states with a weak large-scale ascent (in two simulations) or descent (in four simulations) in column 1.

The simulations initially develop a large-scale circulation with descent in column 1, as would be expected from the difference in initial potential temperature between columns 1 and 2. The resulting rain rate differences are associated with the large-scale circulation. For instance, the large-scale heating and drying in column 1 maintains its initial rain rate below that in column 2, but the rain rate increases rapidly as the strength of the large-scale circulation is reduced. At early times, the evolution of the system in each subset of simulations is very similar. However, shortly after day 7 differences are observed and column 1 evolves toward the three distinct quasi-equilibrium states. Within each quasi-equilibrium state, the variation in large-scale heating rates is about 0.13 mm d^{-1} compared to 0.57 mm d^{-1} between the equilibrium states. There is an equilibrium state with approximately zero large-scale circulation with mean statistics which are very close to those of the RCE state (black curves). The large-scale heating rates for this equilibrium state ranges between -0.06 mm d^{-1} and 0.073 mm d^{-1}. There is also an equilibrium state with a weak large-scale ascent in column 1, with the large-scale heating rates ranging between -0.45 and -0.56 mm d^{-1}, and an equilibrium state with a weak large-scale descent in column 1, with the large-scale heating rates ranging between 0.46 and 0.57 mm d^{-1}. The analysis of the moisture budget shows that the excess or deficit of precipitation at equilibrium is maintained largely by the moisture transport by the large-scale circulation, rather than the difference in surface evaporation (results not shown). These multiple equilibrium states correspond to three distinct equilibria for column 1, but they correspond to two distinct equilibria in the context of the coupled-column system. The mean precipitation rates for these multiple precipitating equilibrium states are within 10% of the value of the RCE state (compare the red and blue curves with the black curve in Figure 3). As a result, the convective state in column 1 is not very different to the RCE state at 302.7 K. Similar multiple precipitating equilibria are obtained in a set of simulations in which column 1 is initialized with instantaneous states at equilibrium of the RCE simulation with an SST of 304.7 K.

Using the WTG approach over uniform surface conditions, multiple equilibria in precipitation have been obtained in both CRMs and SCMs using the reference column approach (Emanuel et al., 2014; Sessions et al., 2010; Sobel et al., 2007), but not always (Daleu et al., 2015a). For two CRMs fully coupled using the WTG approach, Daleu et al. (2012) obtained an equilibrium state with approximately zero large-scale circulation over uniform surface conditions regardless of the initial conditions used. The present study has demonstrated that multiple precipitating equilibria can arise in a two-column configuration when convective properties in each column are determined by an embedded SCM.

4. Transition from Suppressed to Active Convection

In the simulations C, M, and W described in section 3.2, the overturning circulation that is established in the system suppresses convection in column 1. In this section, we perform idealized simulations of a gradually forced transition of convection from that suppressed phase to an active phase.

Table 2

Values of SST (K) for Columns 1 and 2 Before the SST is Changed (SST$_i$) and at the End of Simulations (SST$_f$) for Experiments that Apply the Locally, Remotely and, Locally and Remotely Forced Transitions Methods

Experiments	1	2	3
Methods	Local forcing	Remote forcing	Local-and-remote forcing
SST$_{i_1}$	300.7	302.7	301.7
SST$_{i_2}$	302.7	304.7	303.7
SST$_{f_1}$	302.7	302.7	302.7
SST$_{f_2}$	302.7	302.7	302.7

4.1. Experimental Setup

The simulations of the transition have been performed by adopting the same strategy as in Daleu et al. (2015b). Instantaneous states at equilibrium of the simulations C, M, and W are used as a set of initial conditions for the simulations of the transition. Column 1 is forced to undergo the transition to a more active phase of convection by changing the SSTs toward a uniform value of 302.7 K across the columns. The transition is forced in three different ways: (i) the locally forced experiment, (ii) the remotely forced experiment, and (iii) the locally and remotely forced experiment. The values of SSTs for columns 1 and 2 at the beginning, SST$_i$, and at the end, SST$_f$, of each simulation of the transition are presented in Table 2.

In the locally forced transition, hereafter referred to as experiment 1, five simulations of the transition are performed with the initial conditions taken from five instantaneous states at equilibrium of the simulation C. The SST in column 1 is increased to match the value in column 2 over the course of 1 day. Thus, the transition is driven by a local change in the underlying SST and modulated by the induced change in the strength of the large-scale circulation. In the remotely forced transition, hereafter referred to as experiment 2, five simulations are performed with the initial conditions taken from five instantaneous states at equilibrium of the simulation W. The SST in column 2 is decreased to match the value in column 1 over the course of 1 day. Thus, the transition is driven by a change in the large-scale circulation that is itself is induced by the remote change in SST. Finally, in the locally and remotely forced transition, hereafter referred to as experiment 3, five simulations are initialized from five instantaneous states at equilibrium of the simulation M. The SST in column 1 is increased while simultaneously the SST in column 2 is decreased so as to obtain the same value of 302.7 K in both columns over the course of 1 day.

For each experiment, the five simulations are differentiated by the time at which the SST transition is initialized. Specifically, the transition is initialized at intervals of 2 days and each simulation is run for 75 days from the start of the transition. The results are then combined by defining the start of the SST transition to be time zero.

The strength and the vertical structure of the large-scale circulation, in addition to the mean statistics at equilibrium of the simulations C, W, and M depend only on the SST difference between the two columns (section 3.2). By the end of day 1, the locally, remotely, or the locally and remotely forced transitions have a uniform SST of 302.7 K across the columns. They produce multiple precipitating equilibrium states which are the same as those obtained in section 3.3. As discussed in section 3.3, for these three precipitating equilibrium states the convective state in column 1 is not very different to that of the RCE state at 302.7 K. These similarities are important because they allow the locally, remotely, and the locally and remotely forced transitions to be directly compared.

As in Daleu et al. (2015b), we define the transition time, t^* as a simple measure of the dependency of the transition process on the forcing mechanism. The time t^* is such that

$$RR^{t^*} = \frac{1}{2}(RR^{t<0} + RR^{RCE}), \tag{6}$$

where RR^{t^*} is the rain rate at time t^*. Its value is halfway between the mean rain rates before the SST is changed, $RR^{t<0}$, and at equilibrium, RR^{RCE}.

4.2. Results

In this section, we compare the locally, remotely, and locally and remotely forced transitions by analyzing the transient evolution of convection from its suppressed to its active phase. To do this, we examine the time evolution of precipitation, evaporation, and transport terms, and we also examine the time evolution of the vertical structures of convective properties, humidity, and the WTG vertical velocity. The results presented in this section are computed as a 5 day running mean and a 5 member ensemble mean.

4.2.1. Time Evolution of the Column-Integrated Variables

Figures 4 and 5 present the temporal evolution of column-integrated heating and moistening rates from the large-scale circulation, and the temporal evolution of surface evaporation and rain rates, respectively.
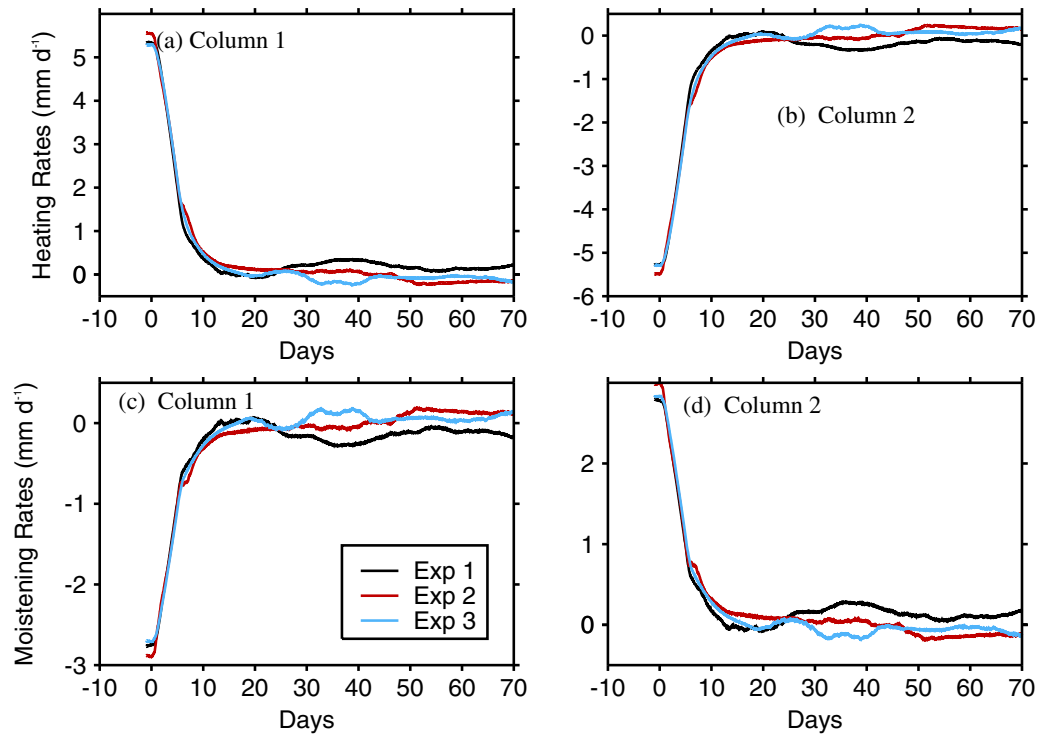
Figure 4. Time evolution of column-integrated (a and b) heating and (c and d) moistening rates from the large-scale circulation. The results are the 5 day running mean and five member ensemble mean for columns (a and c) 1 and (b and d) 2 of experiments 1–3. The heating rate is expressed in millimeters per day via the latent heat of vaporization in order to allow easy comparison.
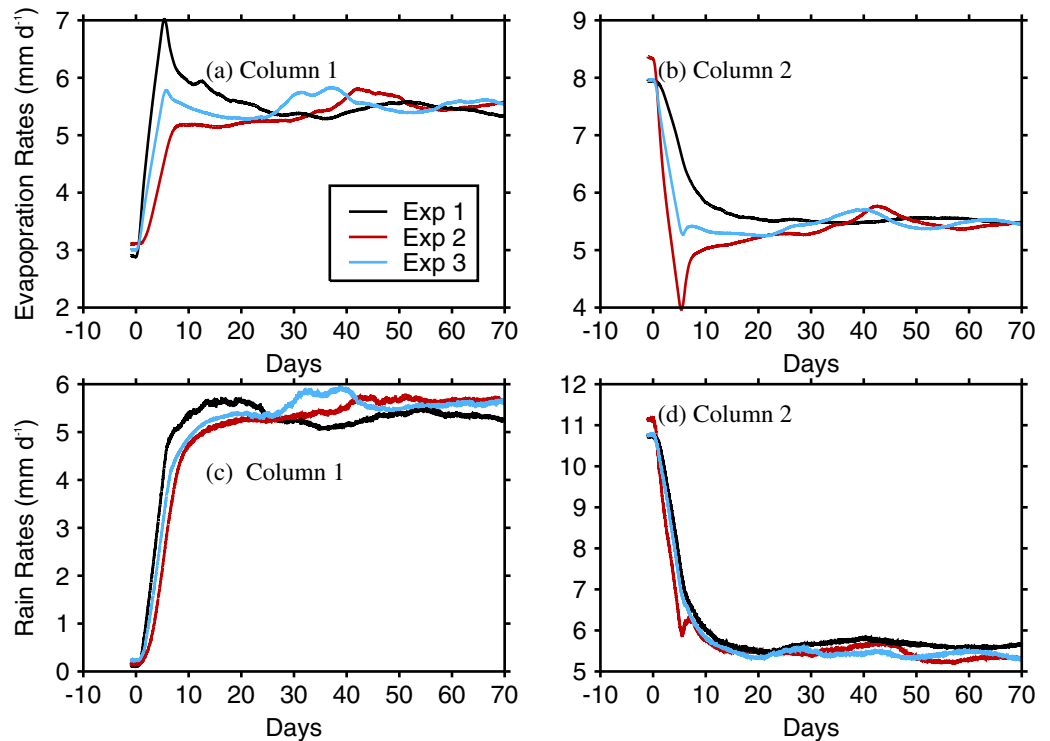

Figure 5. Time evolution of (a and b) surface evaporation and (c and d) rain rates. The results are the 5 day running mean and five member ensemble mean for columns (a and c) 1 and (b and d) 2 of experiments 1–3.
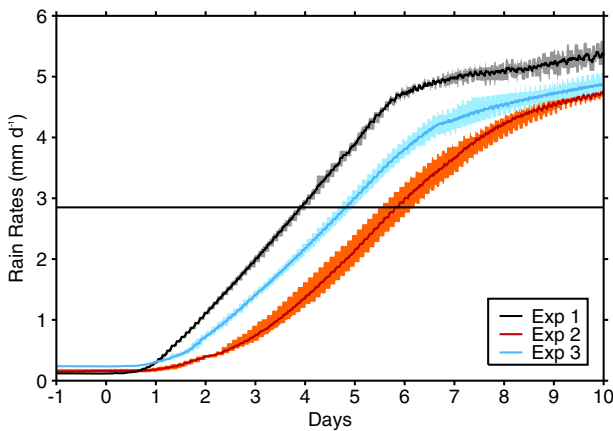
Figure 6. Time evolution of rain rates. The results are the 5 day running mean and 5 member ensemble mean for column 1 of experiments 1–3. The shaded areas represent the range of the five ensemble simulations. The horizontal line represents $RR^{t^*} =$ 2.83 mm d^{-1}.

We expressed the heating rate in millimeters per day via the latent heat of vaporization in order to allow easy comparison.

The simulation of the transition starts at day 0 when the changes in SST produce a reduction in the strength of the large-scale circulation. Despite the fact that the SST in column 1 is equal to the value in column 2 at day 1, the large-scale circulation persists in the system for several days. Over the first few days, the large-scale circulation decreases rapidly and the temporal evolution of the column-integrated heating and moistening rates from the large-scale circulation of these three experiments are very similar (Figure 4). Over a long period of integration, the columns adjust toward precipitating equilibrium states, similar to those found in section 3.3. These figures show the 5 member ensemble mean of the equilibrium states, but within each ensemble all three equilibria can occur as the final state at the end of the transition runs. For example, among the simulations that constitute experiment 1, two achieve an equilibrium state with approximately zero large-scale circulation, while three achieve an equilibrium state with a weak descent in column 1.

From day 0 the temporal evolution of surface evaporation presents significant differences. Surface evaporation in a column with unaltered SST adjusts slowly toward its RCE value (e.g., column 1 of experiment 2). In contrast, when a column is subjected to an SST increase, its surface evaporation increases for an average of about 7 mm d^{-1} over the first day, before decreasing slowly toward the RCE value of about 5.4 mm d^{-1} by day 20 (e.g., column 1 of experiment 1). Similarly, when the column is subjected to an SST decrease, there is a sharp decrease in surface evaporation rate in the first day before recovering to the RCE value (e.g., column 2 of experiment 2).

The temporal evolutions of rain rates for column 1 of experiments 1–3 are presented in Figure 6 and the range of the five ensemble simulations is also shown. The rain rates evolve at different rates, reflecting different forcing mechanisms. From equation (6), RR^{t^*}, the value of rain rate which is halfway in between the value before the SST is changed ($RR^{t<0}$) and the RCE value at 302.7 K (RR^{RCE}) is equal to 2.83 mm d^{-1} (black horizontal line in Figure 6). The values of the transition time for experiments 1–3, t^* are summarized in Table 3. The range of the five ensemble simulations is also listed in square brackets. The locally forced transition method is the most effective transition mechanism. It has a transition time of 3.92 days, almost 2 days faster than that in the remotely forced transition. The value of t^* in experiment 3 is approximately halfway in between the values obtained in experiments 1 and 2.

These results are qualitatively similar to those obtained in the same idealized experimental setup using a CRM (Daleu et al., 2015b), but there are some substantial quantitative differences. For instance, the values of t^* obtained in this study are relatively short compared to the values of 5.4, 10.9, and 8 days obtained for the locally, remotely, and locally and remotely forced transitions performed in Daleu et al. (2015b).

4.2.2. Time Evolution of the Vertical Structures

Column integrated values hide information on the vertical structure. To better understand how these three experiments of the transition differ when using the SCM, we examine time-height cross sections of convective properties, humidity, and the WTG vertical velocity.

Figure 7 presents time-height cross sections in column 1 of the locally forced transition. The results presented are the heating rate from the large-scale circulation and the heating rate from parameterized physics. Here the heating rate from parameterized physics is the sum of heating rates from convection, boundary layer, large-scale cloud, and large-scale rain. The strength of the large-scale circulation decreases rapidly from days 0 to 5. As a result, moisture is rapidly recharged into column 1 (result not shown) and convective cells emerge abruptly with convection reaching the tropopause level (Figure 7c). The strength of the large-scale circulation continues to reduce to nearly zero over a period of about 13 days and a state with substantial deep convection is achieved in column 1 by day 7; at which time the heating rate from parameterized physics reaches 1.2 K d^{-1} at 12 km (see Figure 7c).

Table 3
Transition Time (Days)

Experiments	1	2	3
t^*	3.92	5.88	4.82
	[3.85−4.00]	[5.58−6.19]	[4.65−4.96]

Note. The values between square brackets represent the range of the five ensemble simulations.
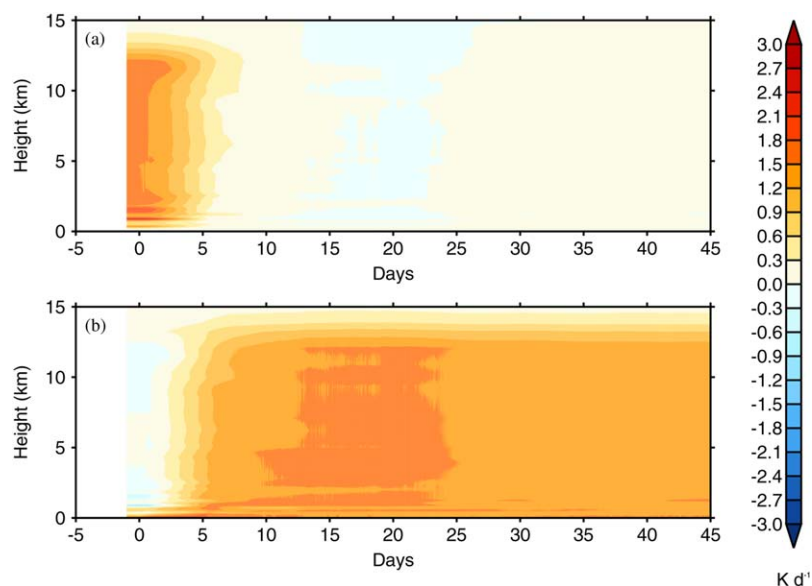
Figure 7. Time-height cross sections for column 1 of experiment 1. Results are the (a) heating rate from the derived large-scale circulation and (b) heating rate from parameterized physics. The heating rate from parameterized physics is the sum of heating rates from convection, boundary layer, large-scale cloud, and large-scale rain. The profiles are the 5 day running mean and five member ensemble mean. The contour intervals are 0.3 K d^{-1} in both panels.

We have compared the evolution of potential temperature and specific humidity in the lowest 2 km in column 1 of experiments 1 and 2 (results not shown). Throughout the integrations, the system in experiment 1 warms and moistens whereas the system in experiment 2 is required to cool and dry to reach very similar equilibrium states. When the SST of a column is increased, its surface evaporation increases rapidly (black curve in Figure 5a) and this contributes to a source of moist static energy in that column and in the two-column system. As a result, convective cells in that column become more active and its boundary layer warms and moistens accordingly. On the other hand, when the SST of a column is decreased, the sharp decrease in surface evaporation contributes to a sink of moist static energy in that column. Thus, its boundary layer cools and dries, and convection is inhibited. In contrast to column 1 of experiment 1 in which the SST is increased, an additional moist static energy source promoting convection is not provided directly in column 1 of experiment 2, since its SST is unaltered. As a result, the inversion at the top of the boundary layer is eroded more rapidly in column 1 of experiment 1 relative to column 1 of experiment 2, suggesting that convection develops more easily within column 1 of experiment 1 relative to column 1 of experiment 2. A similar conclusion was drawn for the corresponding CRM experiments in Daleu et al. (2015b).

Figure 8 presents time-height cross sections in column 1 of the remotely forced transition. Results are the heating rate from the derived large-scale circulation and the heating rate from parameterized physics. This may be compared with the corresponding results for column 1 of the locally forced transition shown in Figure 7. As discussed above, the inversion at the top of the boundary layer is eroded more rapidly in column 1 of experiment 1 relative to column 1 of experiment 2. This delay in column 1 of experiment 2 relative to column 1 of experiment 1 is reflected in other fields. For instance, the large-scale circulation persists for longer in experiment 2 (compare Figure 7a and Figure 8a). In column 1 of experiment 1 convection goes deep abruptly. However, in column 1 of experiment 2, convection reaches the freezing level at first before going deeper a little later, and a state with substantial deep convection is achieved by day 12 compared to day 7 in column 1 of experiment 1 (compare Figure 7c and Figure 8b).

As in Daleu et al. (2015b), the behavior of experiment 3 is somewhere in between those of experiments 1 and 2. For instance, in column 1 of experiment 3 the temporal evolution of surface evaporation rates is in between those of experiments 1 and 2 (Figure 5a) and the analysis of time-height cross section of the heating rate from the parameterized physics (result not shown) reveals that a state with substantial deep convection is achieved by day 9 compared to days 7 and 12 in column 1 of experiments 1 and 2, respectively.

Experiments 1–3 illustrate three different methods of forcing the transition from suppressed to active convection in column 1. Despite the fact that the transition process depends on the forcing mechanism, the
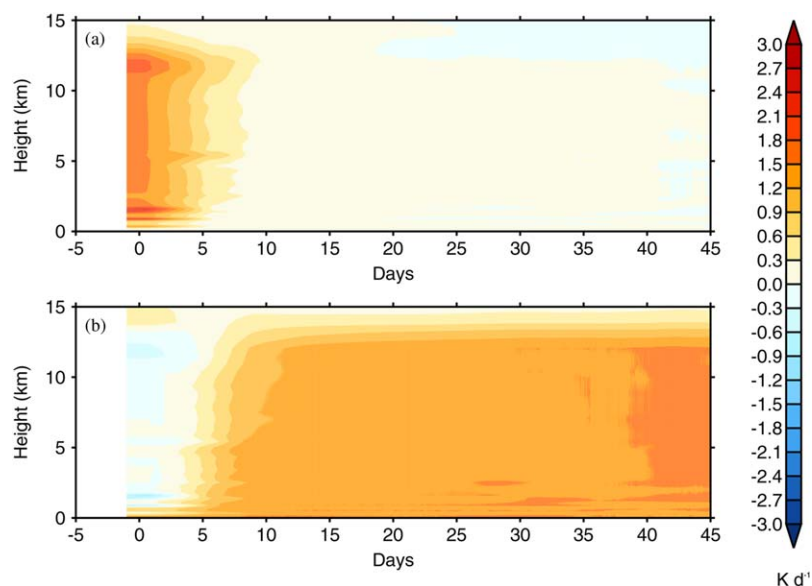
Figure 8. Time height cross sections for column 1 of experiment 2. Results are the (a) heating rate from the derived large-scale circulation and (b) heating rate from parameterized physics. The heating rate from parameterized physics is the sum of heating rates from convection, boundary layer, large-scale cloud, and large-scale rain. The profiles are the 5 day running mean and five member ensemble mean. The contour intervals are 0.3 K d^{-1} in both panels.

common features are that the changes in SST result in diminishing large-scale circulation, and that the transition from suppressed to active convection occurs as the strength of the large-scale circulation decreases.

As for the CRM experiments in Daleu et al. (2015b), the temperature and humidity tendencies due to the evolving large-scale circulation delay the transition to active convection. For instance, the transition time in an experiment that applies the local forcing as in experiment 1 but with the heating and moistening rates from the large-scale circulation switched off instantaneously at day 0 is 2.50 days (see section 5); a value which is 1.42 days faster than that obtained in experiment 1.

4.2.3. The Roles of Surface Forcing and Large-Scale Forcing

As discussed above, the transition to deep convection is delayed considerably when convection is allowed to interact with the large-scale circulation. However, the change in convection within column 1 of experiment 1 is a response to the change in the underlying SST and the resulting change in the strength of the large-scale circulation while that in column 1 of experiment 2 is a response only to the change in the strength of the large-scale circulation. In this section, we isolate the contributions arising directly from the change in SST and the contributions arising from the evolving large-scale circulation.

As in Daleu et al. (2015b), we performed experiments 1a and 2a which are repeated versions of experiments 1 and 2, respectively, but from day 0 the profiles of heating and moistening rates from the large-scale circulation are held fixed to those obtained by averaging over 10 days before the SST is changed. As with the CRM (Daleu et al., 2015b), the transition process never occurs in both cases. Hence, in both models the important mechanism in experiments 1–3 is that the change in SST induces a change in the strength of the large-scale forcing, and it is the latter process that systematically drives the transition to deep convection.

Since the WTG-derived large-scale circulation advects both heat and moisture, we also conducted experiment 1b again following Daleu et al. (2015b) in order to uncouple the contributions from the evolving large-scale heat transport and the evolving large-scale moisture transport. It is a repeated version of experiment 1, but from day 0 the profile of moistening rates from the large-scale circulation is held fixed to the profile obtained by averaging over 10 days before the SST is changed, while the large-scale heating rates remain free to evolve according to the WTG calculations.

Figure 9 shows the evolution of the heating rates from the large-scale circulation, surface evaporation, and rain rates for the dry column of experiments 1 (black curves) and 1b (red curves). The change in SST induces a reduction of the heating rates in both cases. However, a new quasi-equilibrium state is reached in
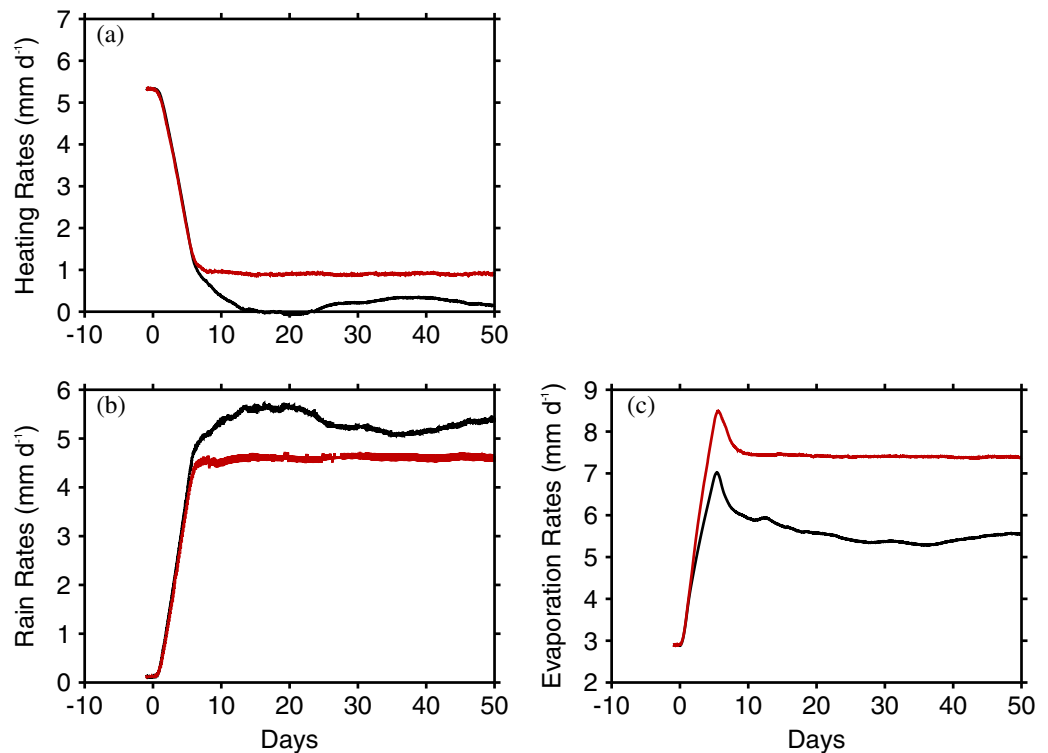
Figure 9. Time evolution of (a) column-integrated heating rates from the large-scale circulation, (b) rain rates, and (c) surface evaporation. Results are the 5 day running mean and five member ensemble mean for the dry column of experiments 1 (black curves) and 1b (red curves). The heating rate is expressed in millimeters per day via the latent heat of vaporization in order to allow easy comparison.

experiment 1b with a mean heating rate of about 1 mm d^{-1} compared to the value of approximately zero in experiment 1. As a result, convection within column 1 of experiment 1b cannot be driven to the same level of activity as that within column 1 of experiment 1. In the column 1 of experiment 1b, the mean rain rate at equilibrium is increased to 4.60 mm d^{-1}, compared to 5.40 mm d^{-1} in column 1 of experiment 1. To balance the imposed drying, surface evaporation is increased by about 4.50 mm d^{-1}, now 7.30 mm d^{-1}.

The value of mean rain rate in column 1 of experiment 1b is 85% of RR^{RCE} while that obtained in an equivalent CRM simulation performed by Daleu et al. (2015b) is 50% of the RCE value in that study. Therefore, in comparison to the CRM in which the heating and moistening effects of the circulations are about equally divided, the heating effects of the circulation dominate in this SCM. This result suggests that this SCM is more able to modify its local evaporation to offset the imposed drying than the CRM.

5. The Effect of Increased Convective Entrainment on the Transition Process

There are marked differences between the results from the SCM (used in this study) and those from the CRM used in the study of Daleu et al. (2015b). As discussed in section 1, the entrainment rate is a parameter in the convection scheme that is well known to be an important source of model uncertainty and to influence the simulation of the tropical mean climate and large-scale variability. We now investigate the effects of increased convective entrainment rate on the transition process in the SCM.

We repeated experiments 1–3 with the entrainment factor F (see definition in section 2.1) increased by 25% (F=1.125), and increased by 50% (F=1.35). The black curves in Figure 10 shows the temporal evolution of rain rates in column 1 of those experiments. Figure 11 shows the corresponding values of t^* as a function of F. It also shows the values of t^* obtained in equivalent experiments using the CRM (Daleu et al., 2015b).

The evolution of convection in column 1 of experiments 1 and 3 is sensitive to F (Figures 11a and 11c, respectively). The stronger the entrainment, the slower the transition process, with the locally forced
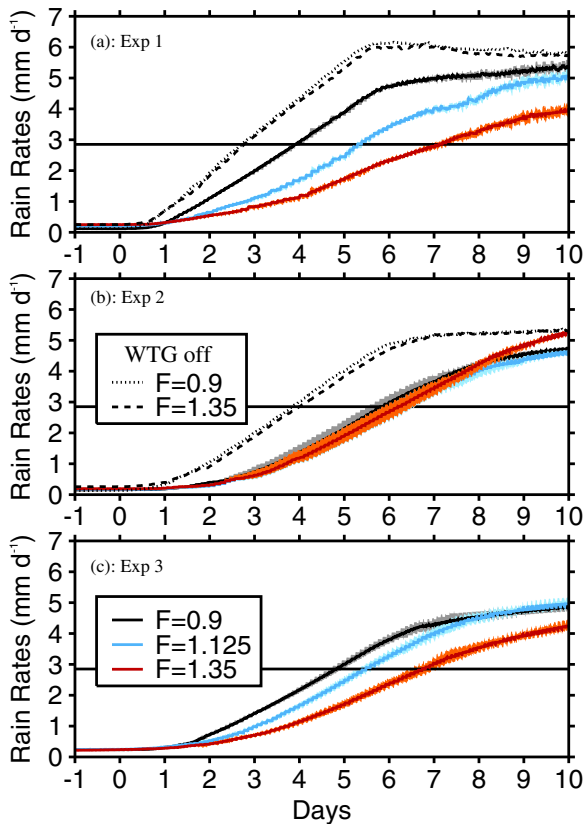
Figure 10. Time evolution of rain rates. The results are the 5 day running mean and five member ensemble mean for column 1 of experiments (a) 1, (b) 2, and (c) 3 with an entrainment factor, F= 0.9 (solid black curves), 1.125 (solid blue curves), and 1.35 (solid red curves). The shaded areas represent the range of the five ensemble simulations. Also shown (dotted and dashed black curves on plots a and b) are the results for column 1 of the experiments that applied the (a) local forcing method and the (b) remote forcing method with F=0.9 (dotted black curves) and F= 1.35 (dashed black curves), but with the heating and moistening rates from the large-scale circulation switched off instantaneously at day 0 when the SST is changed. The horizontal line represents RR^{t^*} =2.83 mm d^{-1}.

transition showing a much wider range of transition times. In contrast, the transition time in experiment 2 is relatively insensitive to F.

The order of the transition times obtained in experiments performed with F=0.9 is identical to that found in equivalent experiments using the CRM (Daleu et al., 2015b), but (as discussed in section 4.2.1) all of the times are faster than in the CRM simulations (compare Figures 11c and 11d). A consequence of the differences in the sensitivity to F is that for F=1.35 the transition times are reordered; the remotely forced transition becomes the fastest because the locally forced transition has become much slower (compare Figures 11a and 11d).

Experiments 1 and 2 achieve very similar equilibrium states, which in turn are very similar to the state obtained in the RCE simulations of the SCM with an SST of 302.7 K. Given that at time 0, column 1 of experiments 1 and 2 are drier than their mean state at equilibrium, the column has to moisten to reach that final equilibrium state. Large-scale advection is a drying tendency for column 1, and although its magnitude is being reduced it remains a drying tendency throughout the transition process. Aside from the reduction in moisture export by the large-scale circulation, the development of deep convection within column 1 of experiments 1 and 2 also depends on the ability of this column to moisten itself. Hence, the only available mechanism to moisten the free troposphere is through convective detrainment of moisture that is lifted from the boundary layer by moist convection. When the entrainment rate is increased (i.e., F=1.35), the detrainment rate is also increased by the same factor (see section 2.1). As a result, for both experiments 1 and 2 the moistening of column 1 through convective detrainment is increased for high entrainment rate (results not shown).

To explore the role of the large-scale circulation in the sensitivity of the transition, we repeated experiments 1 and 2 with low and high entrainment rates (F=0.9 and F=1.35, respectively), but with the heating and moistening rates from the large-scale circulation switched off instantaneously at day 0 when the SST is changed. The red curves in Figure 10 shows the time evolution of rain rate for column 1 of those experiments. For each transition method, the precipitation responses for low and high entrainment rates are very similar. The transition time difference between the low and high entrainment rates is only 0.04 days in the simulations that applied the locally forced transition method and 0.08 days in the simulations that applied the remotely forced transition method. Hence, the simulations of the transitions with low and high entrainment rates differ meaningfully only if convection is allowed to interact with the large-scale circulation.

Figure 12 shows the time-height cross sections of heating rates from convection and heating rates from the derived large-scale circulation for column 1 of experiment 1 with low and high entrainment rates. The results are shown for the first 5 days after the SST is changed. For the low entrainment rate, convection becomes deep quickly (shortly after day 2) as the strength of the large-scale circulation is reduced. In contrast, during the first 5 days for the high entrainment rate, convective cells emerge more gradually and are much shallower with cloud top below 5 km until day 5 (compare Figures 12a and 12b). The precipitation that occurs in column 1 from day 0 (until deep convection is triggered shortly after day 5) is essentially the result of shallow precipitating convection with some contribution (about 30%) from the large-scale rain from stratiform clouds at the top of the boundary layer. For both low and high entrainment rates, convective clouds detrain just above the top of the boundary layer (negative contours in Figures 12a and 12b). However, for the simulation with high entrainment rate, the associated cooling is stronger and it leads to stronger large-scale descent there. Therefore, the difference in the evolution of convection within column 1 of experiment 1 with low and high entrainment rates leads to a difference in the evolution of the large-scale circulation. The large-scale circulation is removed more rapidly in experiment 1 with the low entrainment rate relative to experiment 1 with the high entrainment rate (compare Figures 12c and 12d) and the evolution of convection within the dry column of the simulation that applied the locally forced transition is
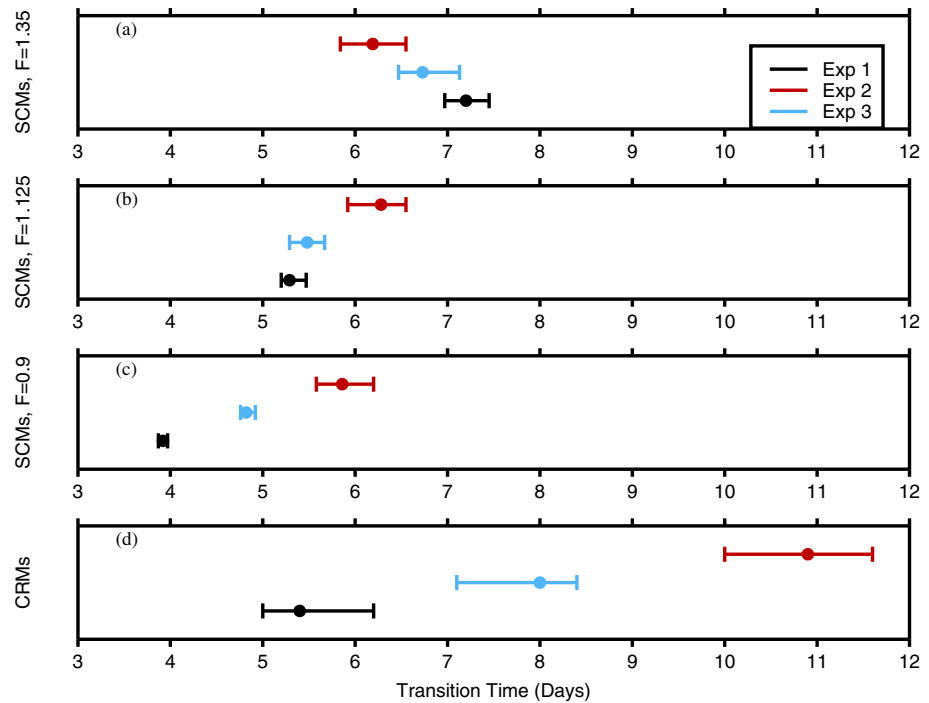
Figure 11. Transition time in column 1 of experiments (black) 1, (red) 2, and (blue) 3. Results are those obtained in experiments performed using the SCM with F= (c) 0.9, (b) 1.125, and (a) 1.35. Also presented are the results obtained in equivalent experiments performed using (d) the CRM (Daleu et al., 2015a). The error bars represent the range of the five ensemble simulations.
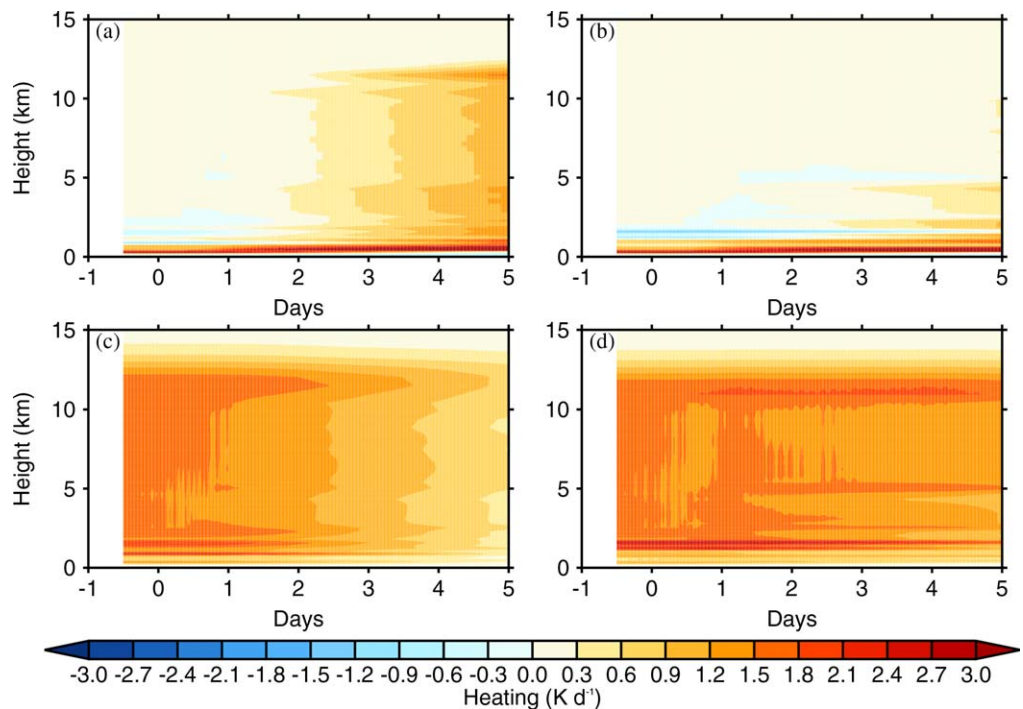

Figure 12. Time-height cross sections of (a and b) heating rates from convection and (c and d) heating rates from the derived large-scale circulation. The profiles are the 5 day running mean and five member ensemble mean for column 1 of experiment 1 with (a and c) F=0.9 and (b and d) 1.35. The contour intervals are 0.3 K d^{-1} in all plots.

controlled not directly by convective detrainment but by how quickly the large-scale circulation is removed from the system.

We analyzed results equivalent to those presented in Figures 12 but for experiment 2. In the remotely forced transition method the rates of change of the large-scale circulation are largely controlled by the reduction in convective activity within column 2 and this is relatively insensitive to the entrainment rate (results not shown). As a result, the evolution of convection within the dry column of the simulation that applied the remotely forced transition is also very similar for the low and high entrainment rates.

6. Conclusions

The WTG approach is used to couple two SCMs using the same configuration as that used by Daleu et al. (2015b) for coupling two CRMs. The coupled SCMs are used to performed idealized simulations of the transition from suppressed to active convection under the influence of the WTG-derived large-scale circulation.

In other studies of the transition from suppressed to active convection, the transition has been forced only by increasing the local surface forcing. The use of the coupled-column model allows us to consider the influence of an evolving large-scale circulation on the transition process. The coupled-column configuration also allows us to study the influence on local convection of changes in remote convection. The sensitivity to changes in convective entrainment rate is explored. The results from the simulations of the transitions performed using a SCM are compared with those obtained from equivalent simulations performed using a CRM (Daleu et al., 2015b).

The simulations of the transition are initialized from coupled-column simulations over nonuniform SSTs, and the column with suppressed convection is forced to undergo the transition to deep convection by changing the SSTs to a uniform value across the two columns. This is done by either increasing the SST in the dry column, decreasing the SST in the wet column, or a combination of both.

The transition time is defined as the time when the rain rate is halfway to the value at equilibrium after the transition. It depends on the forcing mechanism. For the control value of entrainment rate, the transition time is slowest in the simulation that applied the remotely forced transition method and fastest in the simulation that applied the locally forced transition method. The order of the transition times is identical to that obtained in equivalent CRM simulations of the transition (Daleu et al., 2015b) but the times are much faster.

The change in SST does not directly drive the transition and its response is effective during the first few days only. However, it induces subsequent changes in the strength of the large-scale circulation, and it is the evolving large-scale circulation that enables and systematically modulates the transition from suppressed to active convection. In the CRM the contributions of the large-scale circulation are approximately equally divided between the heating and the moistening effects (Daleu et al., 2015b). However, in this study, the contributions from the large-scale circulation are dominated by the heating effects. The relative contributions are 85% and 15% for the heating and moistening effects, respectively. This result was insensitive to increased entrainment rate (not shown) and it was also insensitive to the WTG adjustment timescale. Thus, in comparison to the CRM, the SCM is much more able to modify its local evaporation and maintain convection that offsets an imposed drying.

The transition times in the locally and locally and remotely forced transitions increase with the entrainment rate, with the locally forced transition in particular showing a very strong sensitivity. In contrast, the remotely forced transition is insensitive to increased entrainment rate. In the locally and locally and remotely forced transitions the evolution of convection depends on how quickly the large-scale circulation is removed from the system and the evolution of the large-scale circulation depends on the developing convection in column 1. However, in the remotely forced transition the evolution of the large-scale circulation depends mainly on the reduction in convection in column 2 which appears relatively insensitive to the entrainment rate. As a consequence, increasing the entrainment rate by 50% reorders the rates of the transition in the different experiments. The transition time for the remotely forced transition remains fast while that of the locally forced transition can become slow, in comparison to the CRM (Daleu et al., 2015b).

These results demonstrate that the interactions between convection and large-scale circulation are strongly affected by the entrainment rate. However, while increasing the entrainment rate exerts some influences on the locally forced transition and would allow comparable transition times between CRM and SCM simulations, the

insensitivity of the remotely forced transition means that in the high entrainment rate experiments the sensitivity of the transition time to the forcing mechanism is reversed compared to the CRM. We also explored the sensitivity to the CAPE closure time scale (not shown). The default configuration has a CAPE closure time scale of 30 min and we performed additional simulations with values ranging between 15 and 240 min. The results reveal that the transition process was not sensitive to the CAPE closure time scale, possibly because within the range of values chosen, the CAPE closure time scale is largely controlling the time step intermittency of the convection and not the heating rate averaged over the WTG time scale which controls the evolution of the large-scale circulation.

The WTG approach has been used to extend the traditional SCM and CRM modeling approaches. Importantly, it allows the evaluation of SCM parameterized physics in a simple configuration with two-way interactions between convection and the large-scale forcing. Daleu et al. (2015a, 2016) compared the behavior of a set of SCMs against that of a set of CRMs when the WTG and DGW approaches are used to couple a simulated column to a reference state. This study compares the behavior of a SCM against that of a CRM when the WTG approach is used to couple two simulated columns. This extended framework highlighted a particular sensitivity to a given parameter choice in the convective parameterization scheme that would not have been apparent in a traditional SCM modeling approach.

In this study, we used the WTG approach to extend the traditional SCM modeling approach matching the approach used in the CRM (Daleu et al., 2015b). However, a different parameterization of the large-scale dynamics, including the spectral WTG approach or the DGW approach, can be used and different behaviors may be obtained depending on which large-scale parameterization approach is used. Overall, this study demonstrates that using a large-scale parameterization approach with fully coupled columns may highlight behaviors of the SCM that would not have been found in a traditional SCM setting. Such comparisons between the SCM and the CRM under parameterized large-scale dynamical feedback allow an assessment of the ability of SCM parameterized physics to capture the two-way interactions between convection and large-scale circulations and the results from such an assessment are a useful complement to traditional SCM approaches for developing and testing convective parameterizations.

References

Bretherton, C., & Smolarkiewcz, P. (1989). Gravity waves, compensating subsidence and detrainment around cumulus clouds. *Journal of Atmospheric Sciences*, *46*, 740–759.

Bush, S. J., Turner, A. G., Woolnough, S. J., Martin, G. M., & Klingaman, N. P. (2015). The effect of increased convective entrainment on Asian monsoon biases in the MetUM general circulation model. *Quarterly Journal of the Royal Meteorological Society*, *141*, 311–326.

Daleu, C. L., Plant, R. S., Woolnough, S. J., Sessions, S., Herman, M. J., Sobel, A., . . . van Ulft, L. (2015a). Intercomparison of methods of coupling between convection and large-scale circulation: I. Comparison over uniform surface conditions. *Journal of Advances in Modeling Earth Systems*, *7*, 1576–1601. https://doi.org/10.1002/2015MS000570

Daleu, C. L., Plant, R. S., Woolnough, S. J., Sessions, S., Herman, M. J., Sobel, A., . . . van Ulft, L. (2016). Intercomparison of methods of coupling between convection and large-scale circulation: 2. Comparison over nonuniform surface conditions. *Journal of Advances in Modeling Earth Systems*, *8*, 387–405. https://doi.org/10.1002/2015MS000570

Daleu, C. L., Woolnough, S. J., & Plant, R. S. (2012). Cloud-resolving model simulations with one and two-way couplings via the weak-temperature gradient approximation. *Journal of Atmospheric Sciences*, *69*, 3683–3699.

Daleu, C. L., Woolnough, S. J., & Plant, R. S. (2015b). Transition from suppressed to active convection modulated by a weak temperature gradient-derived large-scale circulation. *Journal of Atmospheric Sciences*, *72*, 834–853.

Davies, T., Cullen, M., Malcolm, A., Mawson, M., Staniforth, A., White, A., & Wood, N. (2005). A new dynamical core for the Met Office's global and regional modelling of the atmosphere. *Quarterly Journal of the Royal Meteorological Society*, *131*, 1759–1782.

Derbyshire, S. H., Maidens, A. V., Milton, S. F., Stratton, R. A., & Willett, M. R. (2011). Adaptive detrainment in a convective parametrization. *Quarterly Journal of the Royal Meteorological Society*, *137*, 1856–1871.

Edman, J. P., & Romps, D. M. (2015). Self-consistency tests of large-scale dynamics parameterizations for single-column modeling. *Journal of Advances in Modeling Earth Systems*, *7*, 320–334. https://doi.org/10.1002/2014MS000378

Emanuel, K., Wing, A. A., & Vincent, E. M. (2014). Radiative-convective instability. *Journal of Advances in Modeling Earth Systems*, *6*, 75–90. https://doi.org/10.1002/2013MS000270

Gregory, D., & Rowntree, P. R. (1990). A mass flux convection scheme with representation of cloud ensemble characteristics and stability-dependent closure. *Monthly Weather Review*, *118*, 1483–1506.

Herman, M. J., & Raymond, D. J. (2014). WTG cloud modeling with spectral decomposition of heating. *Journal of Advances in Modeling Earth Systems*, *6*, 1121–1140. https://doi.org/10.1002/2014MS000359

Holloway, C. E., & Neelin, J. D. (2009). Moisture vertical structure, column water vapor, and tropical deep convection. *Journal of Atmospheric Sciences*, *66*, 1665–1683.

Khairoutdinov, M., & Randall, D. (2006). High-resolution simulation of shallow-to-deep convection transition over land. *Journal of Atmospheric Sciences*, *63*, 3421–3436.

Klingaman, N. P., & Woolnough, S. J. (2014). The role of air-sea coupling in the simulation of the Madden-Julian oscillation in the Hadley Centre model. *Quarterly Journal of the Royal Meteorological Society*, *140*, 2272–2286.

Kuang, Z. (2008). Modeling the interaction between cumulus convection and linear gravity waves using a limited-domain cloud system-resolving model. *Journal of Atmospheric Sciences*, *65*, 576–591.

Kuang, Z. (2011). The wavelength dependence of the gross moist stability and the scale selection in the instability of column-integrated moist static energy. *Journal of Atmospheric Sciences*, *68*, 61–74.

Kuang, Z., & Bretherton, C. S. (2006). A mass-flux scheme view of a high-resolution simulation of a transition from shallow to deep cumulus convection. *Journal of Atmospheric Sciences*, *63*, 1895–1909.

Lin, J.-L., Mapes, B. E., Weickmann, K. M., Kiladis, G. N., Schubert, S. D., Suarez, M. J., . . . Lee, M.-I. (2008). North American monsoon and con- vectively coupled equatorial waves simulated by IPCC AR4 coupled GCMs. *Journal of Climate*, *21*, 2919–2937.

Lock, A. P., Brown, A. R., Bush, M. R., Martin, G. M., & Smith, R. N. B. (2000). A new boundary layer mixing scheme. Part I: Scheme description and single-column model tests. *Monthly Weather Review*, *128*, 3187–3199.

Mapes, B. E. (1997). Equilibrium vs. activation control of large-scale variations of tropical deep convection. R. K. Smith (Ed.), In *The physics and parameterization of moist atmospheric convection* (pp. 321–358). Dordrecht, Netherlands: Springer.

Mapes, B. E., & Houze, R. A. Jr. (1995). Diabatic divergence profiles in western Pacific mesoscale convective systems. *Journal of Atmospheric Sciences*, *52*, 1807–1828.

Masunaga, H. (2012). A satellite study of the atmospheric forcing and response to moist convection over tropical and subtropical oceans. *Journal of Atmospheric Sciences*, *69*, 150–167.

Oueslati, B., & Bellon, G. (2013). Convective entrainment and large-scale organization of tropical precipitation: Sensitivity of the CNRM-CM5 hierarchy of models. *Journal of Climate*, *26*, 2931–2946.

Petch, J. C., Willett, M., Wong, R. Y., & Woolnough, S. J. (2007). Modelling suppressed and active convection. Comparing a numerical weather prediction, cloud-resolving and single-column model. *Quarterly Journal of the Royal Meteorological Society*, *133*, 1087–1100.

Ramsay, H., & Sobel, A. (2011). Effects of relative and absolute sea surface temperature on tropical cyclone potential intensity using a single-column model. *Journal of Climate*, *24*, 183–193.

Raymond, D. J. (2007). Testing a cumulus parametrization with a cumulus ensemble model in weak-temperature-gradient mode. *Quarterly Journal of the Royal Meteorological Society*, *133*, 1073–1085.

Raymond, D. J., & Zeng, X. (2005). Modelling tropical atmospheric convection in the context of the weak temperature gradient approxima- tion. *Quarterly Journal of the Royal Meteorological Society*, *131*, 1301–1320.

Romps, D. (2012a). Weak pressure gradient approximation and its analytical solutions. *Journal of Atmospheric Sciences*, *69*, 2835–2845.

Romps, D. M. (2012b). Numerical tests of the weak pressure gradient approximation. *Journal of Atmospheric Sciences*, *69*, 2846–2856.

Sessions, S. L., Sugaya, S., Raymond, D. J., & Sobel, A. H. (2010). Multiple equilibria in a cloud-resolving model using the weak temperature gradient approximation. *Journal of Geophysical Research*, *115*, D12110. https://doi.org/10.1029/2009JD013376

Sobel, A. H., Bellon, G., & Bacmeister, J. (2007). Multiple equilibria in a single-column model of the tropical atmosphere. *Geophysical Research Letters*, *34*, L22804. https://doi.org/10.1029/2007GL031320

Sobel, A. H., & Bretherton, C. (2000). Modeling tropical precipitation in a single column. *Journal of Climate*, *13*, 4378–4392.

Sobel, A. H., Yuter, S. E., Bretherton, C. S., & Kiladis, G. N. (2004). Large-scale meteorology and deep convection during TRMM KWAJEX. *Monthly Weather Review*, *132*, 422–444.

Stratton, R. A., Stirling, A., & Derbyshire, S. (2009). *Changes and developments to Convective Momentum Transport (CMT) parametrization based on analysis of CRM and SCM* (Tech. Rep. 530). Exeter, UK: Forecsating R&D, Met Office.

Walters, D. N., Best, M. J., Bushell, A. C., Copsey, D., Edwards, J. M., Falloon, P. D., . . . Williams, K. D. (2011). The Met Office Unified Model global atmosphere 3.0/3.1 and JULES global land 3.0/3.1 configurations. *Geoscientific Model Development*, *4*, 919–941.

Wang, S., & Sobel, A. (2011). Response of convection to relative sea-surface temperature: Cloud-resolving simulations in two and three dimensions. *Journal of Geophysical Research*, *116*, D11119. https://doi.org/10.1029/2010JD015347

Wang, S., Sobel, A. H., & Kuang, Z. (2013). Cloud-resolving simulation of TOGA-COARE using parameterized large-scale dynamics. *Journal of Geophysical Research*, *118*, 6290–6301. https://doi.org/10.1002/jgrd.50510

Wang, S., Sobel, A. H., & Nie, J. (2016). Modeling the MJO in a cloud-resolving model with parameterized large-scale dynamics: Vertical structure, radiation, and horizontal advection of dry air. *Journal of Advances in Modeling Earth Systems*, *8*, 121–139. https://doi.org/10.1002/2015MS000529

Webster, P. J., & Lukas, R. (1992). TOGA COARE: The coupled ocean response experiment. *Bulletin of the American Meteorological Society*, *73*, 1377–1416.

Wilson, D. R., & Ballard, S. P. (1999). A microphysically based precipitation scheme for the UK Meteorological Office Unified Model. *Quarterly Journal of the Royal Meteorological Society*, *125*, 1607–1636.

Wilson, D. R., Bushell, A. C., Kerr-Munslow, A. M., Price, J. D., & Morcrette, C. J. (2008). PC2: A prognostic cloud fraction and condensation scheme. I: Scheme description. *Quarterly Journal of the Royal Meteorological Society*, *134*, 2093–2107.

Wu, C. M., Stevens, B., & Arakawa, A. (2009). What controls the transition from shallow to deep convection? *Journal of Atmospheric Sciences*, *66*, 1793–1806.

Yano, J.-I., & Bonazzola, M. (2009). Scale analysis for the large-scale tropical atmospheric dynamics. *Journal of Atmospheric Sciences*, *66*, 159–172.